Nuclear Materials and Energy 25 (2020) 100850

Contents lists available at ScienceDirect

Nuclear Materials and Energy

journal homepage: www.elsevier.com/locate/nme

First exploitation results of recently developed SXR GEM-based diagnostics at the WEST project

Maryna Chernyshova [a,*], Didier Mazon [b], Karol Malinowski [a], Tomasz Czarski [a], Irena Ivanova-Stanik [a], Sławomir Jabłoński [a], Andrzej Wojeński [c], Ewa Kowalska-Strzęciwilk [a], Krzysztof T. Poźniak [c], Philippe Malard [b], Paweł Linczuk [c], Grzegorz Kasprowicz [c], Wojciech Zabołotny [c], Rafał D. Krawczyk [c,d], Piotr Kolasiński [c], Michał Gąska [c], the WEST team [1]

[a] Institute of Plasma Physics and Laser Microfusion, Hery 23, 01-497 Warsaw, Poland
[b] CEA, IRFM, F-13108 Saint-Paul-lez-Durance, France
[c] Warsaw University of Technology, Institute of Electronic Systems, Nowowiejska 15/19, 00-665 Warsaw, Poland
[d] CERN, 1211 Geneva 23, Switzerland

ARTICLE INFO

Keywords:
Nuclear instruments for high-temperature plasma diagnostics
X-ray detectors
SXR plasma spectra modelling
Plasma radiation monitoring
Electron multipliers (gas)
Micropattern gaseous detectors

ABSTRACT

This contribution outlines the first preliminary acquisition data obtained by the GEM diagnostics on WEST. It was designed to monitor the radiation of impurities with a particular focus on the challenges of the elaborated plasma imaging technology in the area of SXR radiation. The details of the developed diagnostics and preliminary results obtained within the commissioning phase of the diagnostics at the WEST Project are provided. It is shown that both spatially and spectrally resolved calibrated data could be collected. A comparison with other WEST diagnostics manifests good qualitative agreement. Currently, the developed system records rather high energy part of the SXR radiation (above 4 keV), that nevertheless still could be useful to assess an intensification of the erosion.

1. Introduction

One of the tasks associated with the study of plasma wall interaction in tokamaks, is to study the process of the formation and behaviour of plasma contamination induced by this interaction. One has to note that plasma contamination can cause many instabilities and may even lead to the disruption of the plasma. Of a particular interest here is tungsten, which is to be used as divertor material in the ITER reactor. Basic information on impurities is, in general, obtained by studying linear emission of their atoms and ions. The solution of most contamination problems depends to a decisive degree on the knowledge of the dynamics of impurities emission in time and space (in the cross-section of the plasma).

X-ray tomography and spectroscopy for getting the knowledge of the dynamics of impurities emission in time and space (in the cross-section of the plasma) are recognized, effective and powerful tools in plasma diagnostics. They provide practical means to study tungsten components erosion, its consequences and material's migration. The search for new technologies in the field of plasma diagnostics entails the increasing demands on the radiative stability of the used materials due to development and usage of fusion facilities, where the study of processes occurring during the interaction of radiation with matter has become particularly important. Currently, a new X-ray imaging detection technology is required for tokamaks such as ITER. X-ray detectors that are being used nowadays in existing equipment may rapidly degrade due to large neutron fluxes characteristic for the D-T and D-D tokamak experiments [1,2]. Recently, new type of detectors has been proposed for plasma physics application [3–6] aiming for the future thermonuclear reactors.

The present work concerns the development of the tomographic system for plasma radiation measurements aimed to be exploited at the WEST project instead of the former SXR diagnostics (DTOMOX [7]). Significant improvements in spatial resolution are expected compared to the former diagnostics with additional, for the first time, photon energy discrimination capabilities to be available in the new system.

The developed system is based on the Gas Electron Multiplier (GEM)

* Corresponding author.
E-mail address: maryna.chernyshova@ipplm.pl (M. Chernyshova).
[1] http://west.cea.fr/WESTteam.

https://doi.org/10.1016/j.nme.2020.100850
Received 31 July 2020; Received in revised form 20 October 2020; Accepted 16 November 2020
Available online 22 November 2020

technology of the modern micropattern gaseous detectors [8]. This type of detectors bases its principle on gaseous multiplication (typically 10^3–10^5 times) of the photoelectrons originated from the incoming ionizing radiation. A typical triple-GEM detector has a layered structure. The gaseous volume is separated by a detector window (that yet serves as a cathode) of 5/0.2 μm thick Mylar/Al, then three GEMs, densely perforated thin Kapton foils each covered with Cu layers on both sides (serving as electrodes), are distanced from the window and each other. The gas chamber is closed by a structured readout board (an anode collecting the generated charge). Irradiation of the detector produces electron signals on its readout electrode. Those signals are then acquired and processed by the dedicated electronics producing pulse-height spectra for each line-of-sight, for the moment, in offline mode. First of two foreseen cameras with 85 lines of sight (LOS) has been installed in the vertical port Q2AH at the WEST project covering conically the divertor view and about one third of edge-to-edge plasma view in the equatorial plane. The reported particular details on the prepared monitoring system could be found in [4,9–14] and references therein.

2. Experimental details

The prepared GEM-based diagnostics system was employed during the last, C4, WEST experimental campaign. The spectra were gathered through 47.3 cm air layer (see Fig. 2 in [4] for the overall layout) between the pinhole and the detector window. That imposes an energy threshold of about 4 keV. The upper recorded photon energy limit is constrained by the detector's efficiency and applied high voltages to the GEM foils (amplification stage of the detector). The detector's centre (pinhole position) is shifted outboard by ~3 cm related to the plasma centre. The system data acquisition was launched by the provided external trigger which was synchronised with other WEST diagnostics. The obtained plasma radiation data could be processed with arbitrary time resolution (down to 10 μs) of the system adjusted to the observed statistics. Two ^{55}Fe gamma sources, permanently mounted in the front of the detector, were used for the energy calibration purposes. A few analysed pulses were characterised by the stable detector amplification, verified by calibration radiation spectra taken before and after a pulse. All the plasma data were collected keeping the similar detector's HV values (providing ~$2{\cdot}10^4$ amplification factor) and the main parameters of the acquisition electronics. Two pulses #54981 and #55166 are presented and discussed here selected based on the diagnostics proper functioning rather than on the detailed physics analysis.

In order to compare the obtained spectra and profiles with other diagnostics the detector's quantum efficiency was calculated by GEANT4 code [15] considering gas working medium and taking into account the entire detector's structure. The detective quantum efficiency (DQE) is shown in Fig. 1 together with the calculated transmission of the air and beryllium window [16] of 50 μm thickness on the pinhole occurring in the front of the detector. As can be seen the spectral sensitivity of the diagnostics for the collected data rises from 4 keV, thus, for the moment it distinguishes rather bremsstrahlung than SXR linear radiation. It should be mentioned that the spectral sensitivity of the SXR diagnostics DTOMOX (taken for comparison) at the horizontal port is in the range of 3–15 keV.

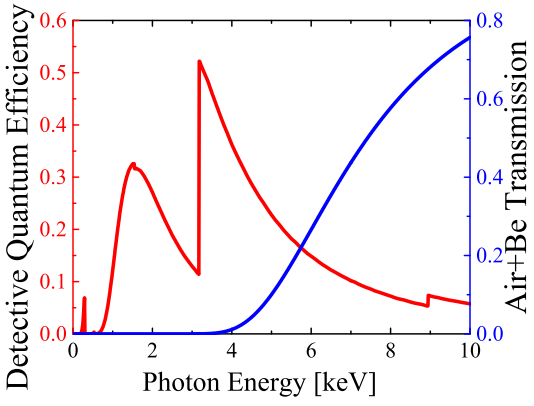

Fig. 1. Calculated DQE of the exploited GEM detector filled with Ar/CO_2 (70/30) gas mixture together with the transmission of the air in the front of the detector and 50 μm Be window on the pinhole.

In Fig. 2 experimental time evolution profiles are shown for #54981, deuterium plasma discharge in L-mode, where Lower Hybrid Current Drive (LHCD) heating was used. The recorded GEM-based diagnostics time profile (integrated over photon energy) is compared to SXR, HXR and neutron data. Different colours on SXR and HXR data correspond to 45 and 38 horizontal LOS, respectively, with the integrated radiation energy. For both pulses maximum intensity of SXR and HXR radiation is revealed by the central LOS. Reasonable agreement was observed between the GEM signal and HXR radiation for this pulse, with some less pronounced relation to SXR data. Two time slices of 50 ms duration were chosen for further analysis: centred at 5 and 8 s at different heating power values of 1.5 and 2.5 MW, respectively.

Similar time traces are shown in Fig. 3 for #55166, L-mode deuterium plasma discharge with Ion Cyclotron Resonance Heating (ICRH). In this case the GEM-based signal could be associated with both SXR and HXR/neutron time traces. Several time slices of 50 ms duration were selected for further analysis: centred at 4, 5.35, 6.8 and 8 s.

It is worth noting that all the photon diagnostics (including the developed one) are of the different spectral response, therefore the immediate connection between them would be barely established.

3. Simulations of the plasma parameters

In order to support the analysis of the obtained experimental data some efforts were taken to simulate the plasma radiation spectra based on the experimental input for a given pulse. First, COREDIV code [17] was used to reproduce the experimental plasma parameters and obtain the missing information about the plasma impurities and their radiation power. The used physical model is based on a self-consistent coupling of the radial transport in the core to the 2D multifluid description of the scrape-off layer (SOL). In the core plasma, the 1D radial transport equations for bulk ions, for each ionization state of impurity ions and for the electron and ion temperature, are solved. Whereas in the SOL the 2D boundary layer code EPIT was used, primarily based on Braginskii-like equations for the background plasma and on rate equations for each ionization state of each impurity species. The sputtering processes of tungsten at target plate are taken into account. The results include the existence of the self-regulating mechanism, which couples the tungsten production at the target with the W radiation in the core.

COREDIV simulations for each of the considered pulses were performed assuming only three main impurities are expected to be present (i.e., observed experimentally) in the plasma, namely, N, O and W, with negligible amount of Ni. Since the energy balance depends strongly on the coupling between the bulk and the SOL plasma, modelling requires the transport problem to be addressed in both regions simultaneously. This is more important for the WEST project, where tungsten is produced by plasma-wall interaction and is a source of radiation emission from the core plasma. The joined treatment of both regions is necessary as long as the edge plasma is not separated from the bulk plasma.

Since the model is relatively complex, only the aspects relevant to the present study are pointed out. Some differences in the similar simulations for the other tokamaks could be noticed. For the auxiliary heating parabolic-like deposition profile is assumed to be $P_{AUX} = P_0(1\text{-}r^2/a^2)^y$, where r is the radial coordinate, a - the plasma radius and y is usually in the range of 1.5–3 for JET-ILW discharges [18–20] and ASDEX-Upgrade [21]. For the reported here simulations $y = 30$ for pulse #54981 (LHCD heating) and $y = 10$ for #55166 (ICRH heating) were used chosen based on the very strong peaking profile of the heating. Another important

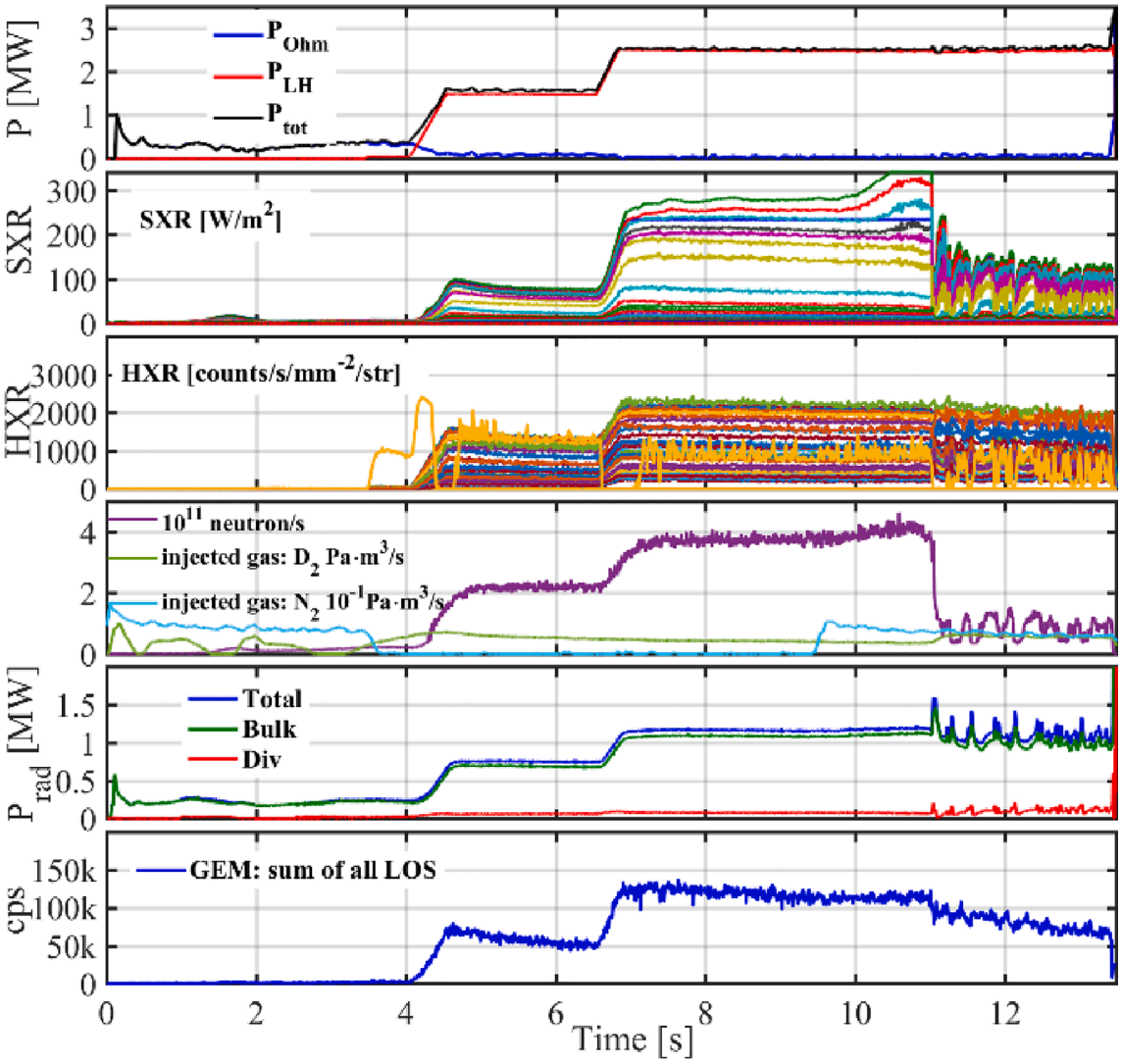

Fig. 2. Experimental time traces for pulse #54981 with GEM-signal at the bottom of 10 ms time resolution.

condition was an absolutely necessary assumption that 90% or 80% of the auxiliary heating runs up to electrons for #54981 or #55166, respectively. Only in that way the experimental ratio of the electron and ion temperature, as well as their profiles, could be reconstructed with an acceptable agreement.

The energy losses are mainly determined by bremsstrahlung, ionization and line radiation. In the SOL, the 2D fluid equations are solved in the simplified slab geometry but taking into account plasma recycling in the divertor and sputtering processes due to all considered ions at the target plate. The sputtered W fluxes should be treated as averaged within the time interval (over 1–2 s) whereas comparison with experimental data should be reasonable only for the steady state discharges. The code was run with the density value at the separatrix (an input parameter for the simulation) taken from the experimental data, assuming to be about 30% of the average volume density. The radial transport in the SOL was fixed by $D_{SOL} = 0.5$ m^2/s.

Three main impurities were considered: N, O, W (together with very low nickel concentration of 1–5 10^{-4} to account for presence of mid-Z impurities) assuming the ratio of N to O being 10%. In the applied approach determination of the proportions between different impurities was aimed to reproduce the observed total radiation power whose solution is not unambiguous. In Figs. 4 and 5 the obtained total radiation is shown together with the distribution of ionisation state for the pulses #54981 and #55166, respectively.

For the two compared time slices for pulse #54981 that differ in the LHCD heating power, the average plasma electron density remains almost the same with increased T_e for higher power. The total radiation from the bulk plasma is dominated by W line radiation for both time slices. Its radiation is peaked for #54981 at the mid-radius ($r/a \approx 0.35$ for 5 s and 0.45 for 8 s, Fig. 4). The radiation maximum shift in the radial position between two time slices is in correspondence with the electron temperature profiles at 5 and 8 s, considering that W cooling rate is peaked in 1–2 keV region. The achieved simulated W density profiles (not presented here) for pulse #54981 showed wide plateau in the core plasma, more pronounced for 5 s than for 8 s. An increase of the calculated W concentration from $C_W = 1.36 \cdot 10^{-2}$ to $2.14 \cdot 10^{-2}$ for 5 s and 8 s, respectively, is associated with an increase of LHCD heating from 1.5 MW to 2.5 MW.

For the second pulse, #55166, calculated tungsten concentration is $C_W = 1.26 \cdot 10^{-3}$ for 5.35 s and is 10^2-10^3 times lower for other time slices. Therefore, the core plasma radiation is dominated by W line emission only for 5.35 s. For 4 and 8 s the core plasma radiation is determined by bremsstrahlung, which is competitive to line radiation for 6.8 s. As can be seen (Figs. 4 and 5, top graphs) the most prominent W ions are $W^{+31\text{-}34}$ for both pulses.

The obtained impurity concentration profiles were used as an input for further calculations of the SXR spectra.

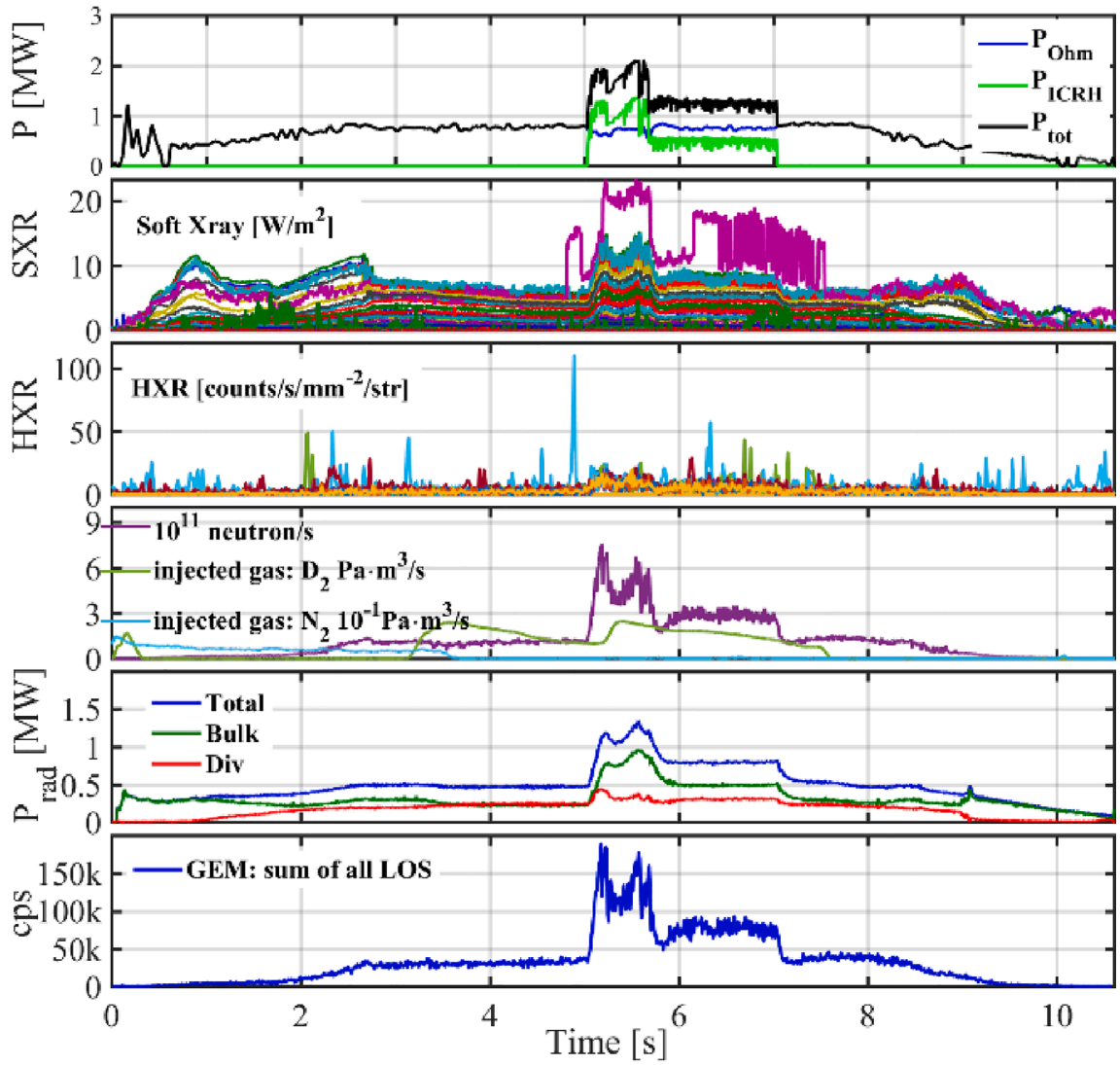

Fig. 3. Experimental time traces for pulse #55166 with GEM-signal at the bottom of 10 ms time resolution.

4. Details on simulation of the plasma radiation spectra

Using the coronal equilibrium assumption an overall assessment of the photons observed by each of the diagnostics' LOS can be made. In the case of more advanced calculations such as, e.g., in tomographic reconstructions of the plasma parameters where the detailed knowledge about impurities distribution is important, transport effects should be taken into account. It is especially important but difficult to realize in the case of tungsten transport modelling where very often advanced GKW and neoclassical calculations are used. However, even simplified but fast calculations, based on the coronal balance model, can provide answers to questions related to the load of SXR diagnostics pixels and, thus, contribute in the development and commissioning phases of the new types of detectors built for specific plasma devices.

With this in mind, the obtained by means of COREDIV simulated impurities profiles were used together with the experimental electron density n_e and electron temperature T_e data in order to estimate the foreseen spectra on the SXR detector. Here, the calculations based on the theory presented in [22] were performed taking into account geometry of the detector, its size and location relative to the plasma as well as the size, shape and position of the pinhole. As a result, an X-ray spectrum for each pixel of the GEM detector is generated. Three main mechanisms of soft X-ray emission are considered [22]: free-free emission (bremsstrahlung); free-bound emission (recombination radiation), bound–bound emission (line radiation).

The calculations require 2D input data of $T_e(R)$ and $n_e(R)$. The last one represents content of electrons origin from all the ionic components of the plasma for each point along the radius, R. Here, the simulations were based on the experimental $T_e(R)$ and $n_e(R)$ profiles as well as with the use of density profiles for each ionic impurity along R, ($n_W(R, Z_j)$, $n_O(R, Z_j)$, $n_N(R, Z_j)$, $n_{Ni}(R, Z_j)$) provided by COREDIV code.

For two considered pulses (#54981, #55166) calculations were performed taking into account geometrical parameters of the exploited GEM detector (dimensions of the pixels (LOS), relative positions of LOS to the pinhole and pinhole position to the plasma centre, etc.) and information on plasma composition (amount of impurities relative to the electron density) with the generated 2D profiles (from the experimental 1D ones) of the electron density and temperature. Calculations were made for H plasma instead of D considering that this has a negligible effect on the results and allows accessing essential parameters, e.g., effective ionisation and recombination coefficients, from the available databases. Based on these data and assuming the local charge balance, fractional abundances and densities for all the impurity ions were calculated.

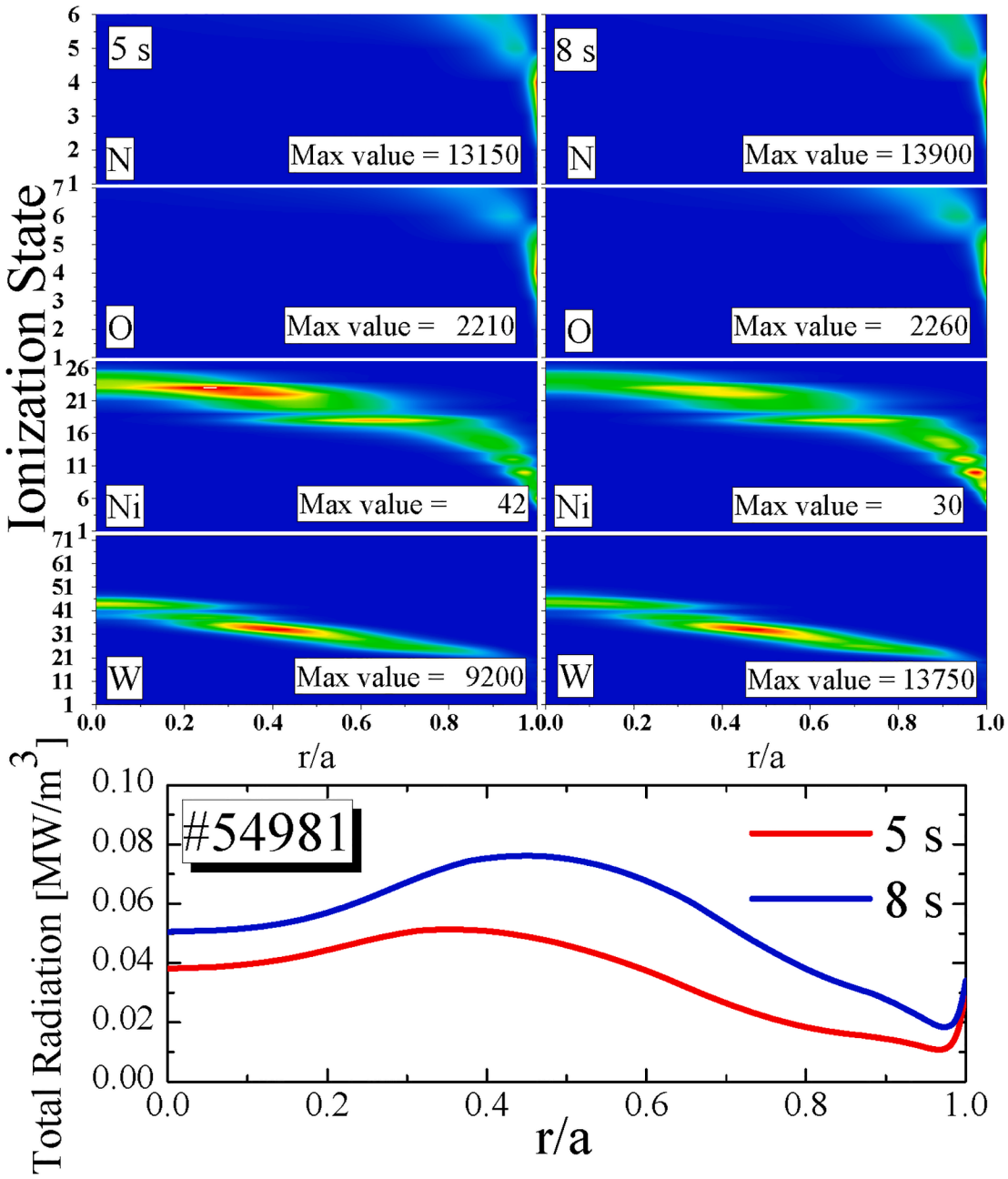

Fig. 4. #54981 pulse: (top graphs) radial distributions of the impurity ionisation states (colour scale: blue - 0; red - specified max value); (bottom graph) total radiation profiles. (For interpretation of the references to colour in this figure legend, the reader is referred to the web version of this article.)

5. Comparison of the experimental data and simulation results

In Fig. 6 the radiation spatial and spectral distributions, both experimental and simulated, are shown for two considered pulses. It can be observed (Fig. 6(a)) that the measured spatial distribution for #54981 confirms that radial radiation profile is peaked at the mid-radius, as the first and last (more pronounced due to the shift relating to the plasma centre) vertical channels exhibit a slight intensity shoulder. That is, however, not reflected for the calculated spatial distribution (Fig. 6(c)). It is slightly more pronounced for 5 s than for 8 s, that would be in agreement with the radiation maximum shift for the second time slice to a larger *r/a*. The observed slightly asymmetric radial profile might correspond to the plasma shape that is enhanced by the shifted pinhole regarding the plasma centre (at 38-th channel). Nevertheless, this asymmetry is much more pronounced for #54981 than for #55166 (Fig. 6(a, e)), whose spatial distribution manifests almost symmetric shape around 45-th channel, although shifted relating to the plasma centre.

The spectral distributions for both pulses, integrated within the whole detector, have a low energy shoulder (Fig. 6(b, f)). Its origin is unlikely coming from low energy photons within the present experimental setup, behind almost 50 cm of air. Such a shoulder, in this case, could result from interaction of high energy ionizing radiation with the detector working gas and materials (see, e.g., [11]). This shoulder is broader in case of #54981, suggesting more intensive background radiation. It could be expected for LHCD experiments in tokamaks where fast electron bremsstrahlung was recognized. Higher HXR content for this pulse is also provided by regular HXR diagnostics at WEST contrary to #55166 with ICRH heating (see Figs. 2 and 3). The higher radiation energy the lower charge/signal is released in the gas volume of the

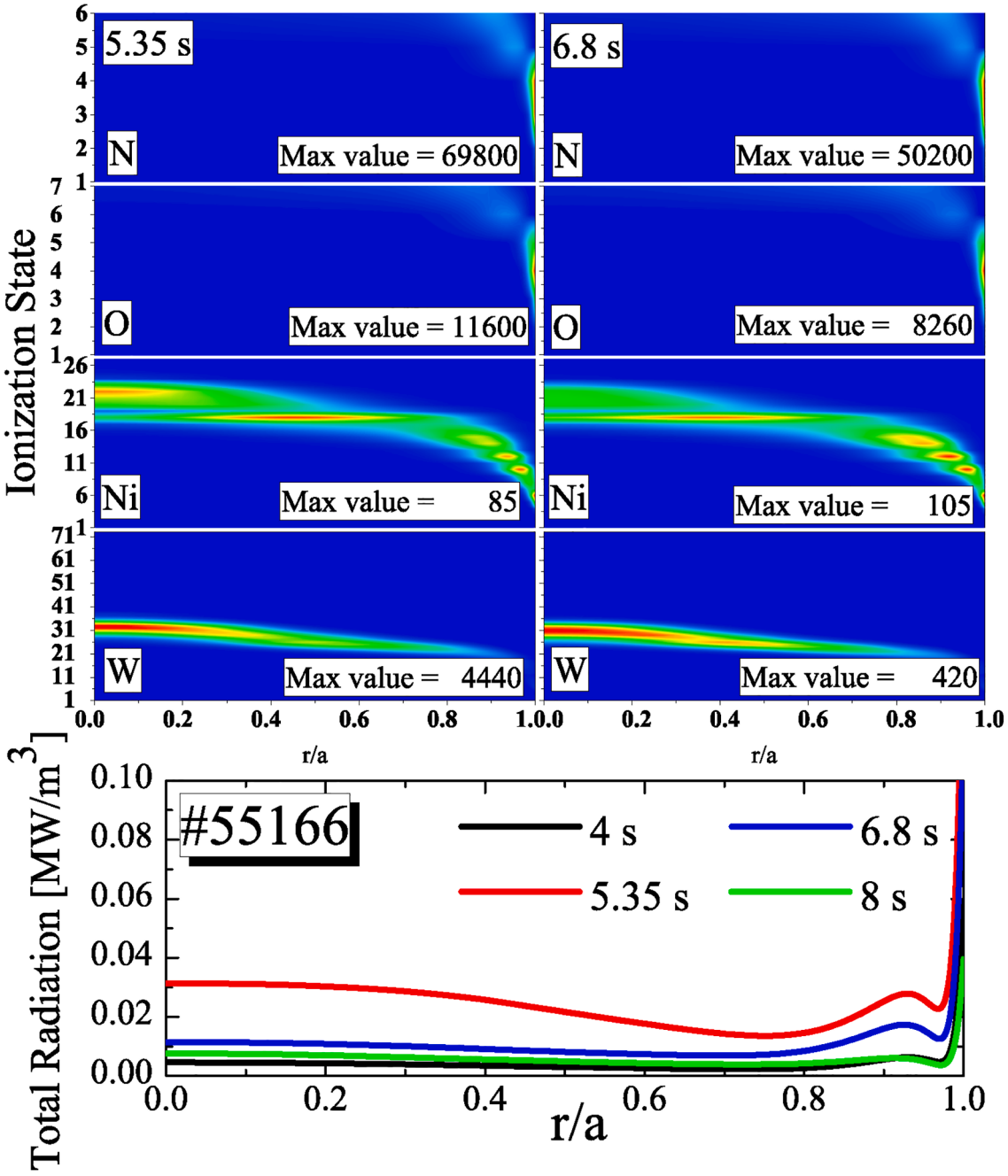

Fig. 5. #55166 pulse: (top graphs) radial distributions of the impurity ionisation states (colour scale: blue - 0; red - specified max value); (bottom graph) total radiation profiles. (For interpretation of the references to colour in this figure legend, the reader is referred to the web version of this article.)

detector. A signature of the higher energy photons passing through the detector for #54981 is also a weak feature at about 8 keV, present for 8 s data (Fig. 6(b)). It points onto Cu *K*-series fluorescence from the GEM foils, where Cu excitation takes place starting at ~ 9 keV, the copper absorption edge. Therefore, it could be assumed that the total detector signal is composed of two components: the direct SXR radiation and high energy radiation products coming from high energy quanta interaction with the surroundings. The later occurred to be more intensive for #54981 than the higher energy part (above 4–5 keV) of the SXR spectrum. This corresponds to the calculations results, that for this pulse the total radiation of the bulk plasma is dominated by the line radiation of W (COREDIV output), which is barely recordable within the present experimental set-up. Additionally, the obtained from calculations bremsstrahlung part is almost two times smaller for #54981 than for #55166, thus it is also not clearly recognizable in the measured spectrum due to the low statistics. It is expected that the ratio between two components of the recorded spectrum will be much more profitable regarding the SXR intensity in the presence of He buffer in the front of the detector instead of the air gap.

For #55166 the spatial distribution (Fig. 6(e)) is strongly localized outwards the plasma centre. This could be related with a plateau on the electron temperature profiles for the core plasma and temperature drop starting from $r/a \approx 0.2$. The radiation distribution maximum is shifted towards LFS, although the magnetic axis for the both pulses was the same. For this pulse the spectral distribution does not reveal so wide low energy shoulder as for #54981. It points onto much weaker presence of higher energy radiation, what is confirmed also from comparison between available HXR data (Figs. 2 and 3) for two selected pulses, as

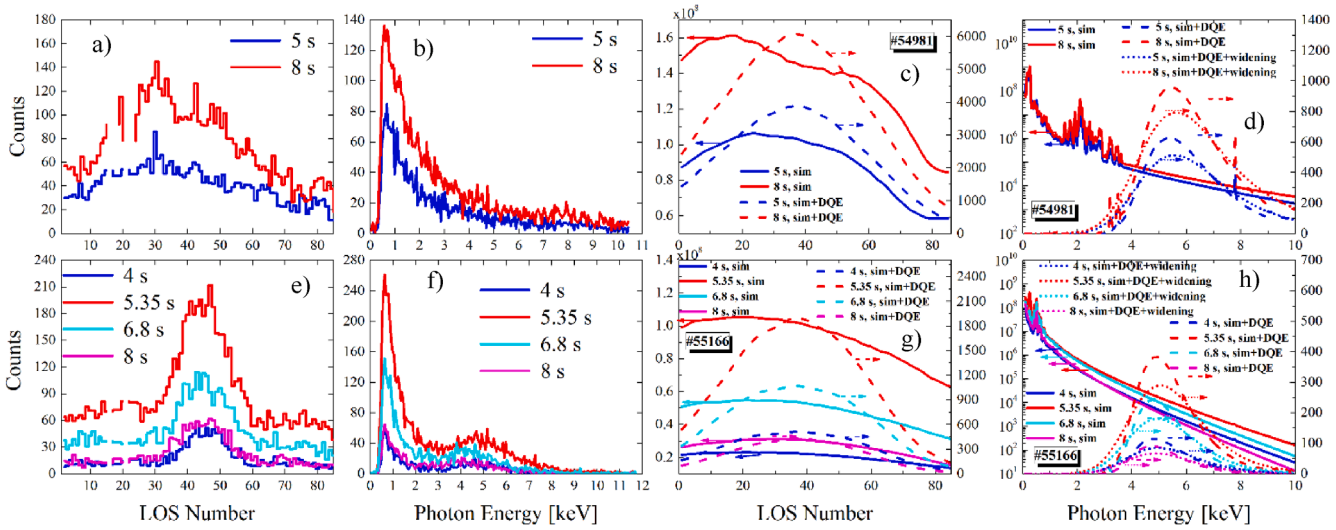

Fig. 6. Experimental spectral and spatial radiation distributions of 50 ms exposure time, collected by GEM-based diagnostics, for two considered pulses (a, b, e, f) together with the simulated data (c, d, g, h). "*Sim*" refers to the initial calculated spectra and spatial distributions, "*sim* + *DQE*" – to the input spectra affected by the air layer/Be window transmission and the GEM detector efficiency and "*sim* + *DQE* + *widening*" – to the final widening of the spectra due to the detector energy resolution. The first channel corresponds to the High Field Side (HFS), the last, 85-th, channel - to the Low Field Side (LFS). The y-axis on all figures is for counts per 50 ms duration.

already was noticed. Wide peak starting at about 4 keV could be associated with the bremsstrahlung radiation with the time trace following rather the SXR data. As it was obtained from COREDIV simulation results, the total radiation from the bulk plasma (r/a = 0–0.4) is dominated by bremsstrahlung at 4 and 8 s, which is comparable with the line radiation at 6.8 s and is much smaller than the line radiation at 5.35 s. Nevertheless, the GEM-based diagnostics recorded rather bremsstrahlung than line radiation in the SXR region for this pulse, what is manifested by the presence of the wide peak at 5 keV (see Fig. 6(f)), whose relative intensities for all the time slices follow the same trend as the simulation results (compare it with the peak at 5 keV in Fig. 6(h)).

It is worth noting that for the mostly ohmic helium-deuterium plasma such a low energy shoulder was not observed for the recorded pulses. The obtained spectra followed quite well the air layer transmission with the radiation intensity starting from 4 to 5 keV decaying towards higher photon energy. Negligible traces of the high energy particles (appeared as presence of the low energy shoulder) were observed for these cases. As for the spatial radiation distribution for such pulses, LFS SXR radiation localisation was noticed.

It is worth adding that, after the validation of the diagnostics data, applying the synthetic diagnostics will help revealing more detailed picture of the impurity radiation spatial and spectral distribution.

6. Summary

The first results were obtained by recently developed SXR diagnostics for the WEST project based on the new type of gaseous detectors. It is shown that both spatially and spectrally resolved calibrated data could be collected. To support the obtained experimental results simulations of the plasma impurity parameters and spectra were conducted. The measured spectra present the combined contribution from both the SXR and high energy ionizing radiation. A comparison with other WEST diagnostics manifests good agreement in trends. At the present set-up of the diagnostics the system records rather high energy part of the SXR and is sensitive to the high ionizing radiation. The gathered data, shown for two selected pulses, followed well the bremsstrahlung and high energy radiation behaviour. The direct SXR measurements are planned to be conducted during the next experimental campaign applying the developed synthetic diagnostics.

CRediT authorship contribution statement

Maryna Chernyshova: Conceptualization, Methodology, Supervision, Investigation, Validation, Visualization, Project administration, Writing - original draft, Writing - review & editing. **Didier Mazon:** Resources, Validation, Investigation, Writing - original draft. **Karol Malinowski:** Investigation, Validation, Formal analysis, Software, Data curation. **Tomasz Czarski:** Software, Validation, Investigation, Data curation, Formal analysis. **Irena Ivanova-Stanik:** Methodology, Software, Validation, Visualization, Formal analysis, Writing - original draft. **Sławomir Jabłoński:** Software, Validation, Visualization, Formal analysis, Writing - original draft. **Andrzej Wojeński:** Software, Resources, Data curation, Validation, Investigation. **Ewa Kowalska-Strzęciwilk:** Visualization, Resources. **Krzysztof T. Poźniak:** Software, Resources, Data curation. **Philippe Malard:** Resources, Investigation. **Paweł Linczuk:** Software, Resources, Data curation, Investigation. **Grzegorz Kasprowicz:** Software, Resources. **Wojciech Zabołotny:** Software, Resources. **Rafał D. Krawczyk:** Software, Resources. **Piotr Kolasiński:** Software, Resources, Data curation. **Michał Gąska:** Resources. **:** .

Declaration of Competing Interest

The authors declare that they have no known competing financial interests or personal relationships that could have appeared to influence the work reported in this paper.

Acknowledgments

This work has been carried out within the framework of the EUROfusion Consortium and has received funding from the Euratom research and training programme 2014-2018 and 2019-2020 under grant agreement No 633053. The views and opinions expressed herein do not necessarily reflect those of the European Commission.

This scientific work was partly supported by the Polish Ministry of Science and Higher Education within the framework of the scientific financial resources in the year 2020 allocated for the realization of the international co-financed project No 5118/H2020/EURATOM/2020/2.

References

[1] F.H. Seguin, et al., Radiation-hardened X-ray imaging for burning-plasma tokamaks, Rev. Sci. Instrum. 68 (1) (1997) 753.
[2] A. Huber, et al., Response of the imaging cameras to hard radiation during JET operation, Fusion Eng. Des. 123 (2017) 669.
[3] M. Chernyshova, et al., Development of GEM gas detectors for X-ray crystal spectrometry, JINST 9 (2014) C03003.
[4] M. Chernyshova, et al., Conceptual design and development of GEM based detecting system for tomographic tungsten focused transport monitoring, JINST 10 (2015) P10022.
[5] D. Mazon, et al., GEM detectors for WEST and potential application for heavy impurity transport studies, JINST 11 (2016) C08006.
[6] F. Cordella, et al., Results and performances of X-ray imaging GEM cameras on FTU (1-D), KSTAR (2-D) and progresses of future experimental set up on W7-X and EAST facilities, JINST 12 (2017) C10006.
[7] D. Mazon, et al., Soft X-ray tomography for real-time applications: present status at Tore Supra and possible future developments, Rev. Sci. Instrum. 83 (2012), 063505.
[8] F. Sauli, The gas electron multiplier (GEM): Operating principles and applications, Nucl. Instrum. Method A 805 (2016) 2–24.
[9] M. Chernyshova, et al., GEM detector development for tokamak plasma radiation diagnostics: SXR poloidal tomography, Proc. SPIE 9662 (2015), 966231.
[10] D. Mazon, et al., Design of soft-X-ray tomographic system in WEST using GEM detectors, Fusion Eng. Des. 296–97 (2015) 856.
[11] M. Chernyshova, et al., Gaseous electron multiplier-based soft X-ray plasma diagnostics development: preliminary tests at ASDEX Upgrade, Rev. Sci. Instrum. 325 (2016).
[12] D. Mazon, et al., SXR measurement and W transport survey using GEM tomographic system on WEST, JINST 12 (2017) C11034.
[13] T. Czarski, et al., The cluster charge identification in the GEM detector for fusion plasma imaging by soft X-ray diagnostics, Rev. Sci. Instrum. 87 (2016) 11E336.
[14] A. Wojenski, et al., Multichannel measurement system for extended SXR plasma diagnostics based on novel radiation-hard electronics, Fusion Eng. Des. 123 (2017) 727.
[15] S. Agostinelli, et al., Geant4 – A simulation toolkit, Nucl. Instrum. Method A 506 (2003) 250.
[16] https://henke.lbl.gov/optical_constants/.
[17] R. Zagorski, et al., Simulations with the COREDIV code of DEMO discharges, Nucl. Fusion 53 (2013), 073030.
[18] G. Telesca, et al., Numerical simulations of JET discharges with the ITER-like wall for different nitrogen seeding scenarios, J. Nucl. Mater. 463 (2015) 577.
[19] I. Ivanova-Stanik, et al., COREDIV and SOLPS numerical simulations of the nitrogen seeded JET ILWL-mode discharges, Contrib. Plasma Phys. 56 (6–8) (2016) 760.
[20] R. Zagorski, et al., Influence of seeding and SOL transport on plasma parameters in JET ITER-like wall H-mode discharges, J. Nucl. Mater. 463 (2015) 649.
[21] K. Galazka, et al., Numerical simulations of JET discharges with the ITER-like wall for different nitrogen seeding scenarios, Contrib. Plasma Phys. 56 (6–8) (2016) 772.
[22] S. Jablonski, et al., Simulation of pulse height analysis soft X-ray spectra expected from W7-X, JINST 10 (2015) P10021.